
This is an electronic reprint of the original article.
This reprint may differ from the original in pagination and typographic detail.

Wu, Zekun; Wang, Tianzuo; Zou, Ji Jun; Li, Yongdan; Zhang, Cuijuan

Amorphous Nickel Oxides Supported on Carbon Nanosheets as High-Performance Catalysts for Electrochemical Synthesis of Hydrogen Peroxide

Published in:
ACS Catalysis

DOI:
[10.1021/acscatal.2c01829](https://doi.org/10.1021/acscatal.2c01829)

Published: 20/05/2022

Document Version
Peer-reviewed accepted author manuscript, also known as Final accepted manuscript or Post-print

Published under the following license:
Unspecified

Please cite the original version:
Wu, Z., Wang, T., Zou, J. J., Li, Y., & Zhang, C. (2022). Amorphous Nickel Oxides Supported on Carbon Nanosheets as High-Performance Catalysts for Electrochemical Synthesis of Hydrogen Peroxide. *ACS Catalysis*, 12(10), 5911-5920. <https://doi.org/10.1021/acscatal.2c01829>

This material is protected by copyright and other intellectual property rights, and duplication or sale of all or part of any of the repository collections is not permitted, except that material may be duplicated by you for your research use or educational purposes in electronic or print form. You must obtain permission for any other use. Electronic or print copies may not be offered, whether for sale or otherwise to anyone who is not an authorised user.

Amorphous nickel oxides supported on carbon nanosheets as high performance catalysts for electrochemical synthesis of hydrogen peroxide

Zekun Wu^{a,b}, Tianzuo Wang^{a,b}, Ji-Jun Zou^{a,b,*}, Yongdan Li^{a,b,c}, Cuijuan Zhang^{a,b*}

^a State Key Laboratory of Chemical Engineering, Tianjin Key Laboratory of Applied Catalysis, Science and Technology, School of Chemical Engineering and Technology, Tianjin University, Tianjin 300072, China. Email: cjzhang@tju.edu.cn

^b Collaborative Innovation Center of Chemical Science and Engineering (Tianjin), Tianjin 300072, China

^c Department of Chemical and Metallurgical Engineering, School of Chemical Engineering, Aalto University, Kemistintie 1, Espoo, P.O. Box 16100, FI-00076, Aalto, Finland.

KEYWORDS: *hydrogen peroxide, electrocatalysis, oxygen reduction reaction, amorphous, nickel oxide, mesoporous carbon*

ABSTRACT: The development of high performance yet cost-effective catalysts for electrochemical synthesis of H₂O₂ is a great challenge. Here, the amorphous nickel oxide NiO_x supported on carbon nanosheets was prepared by the photochemical metal organic deposition method. The evolution of crystalline structure, microstructure, and 2-electron oxygen reduction reaction (2e-ORR) activity in 0.1 M KOH was systematically investigated. The results reveal that the amorphous NiO_x is highly efficient and selective towards 2e-ORR, with onset potential of 0.76 V vs. reversible hydrogen electrode (RHE), 91% selectivity and electron transfer number of ~2.2 over a wide potential range of 0.15-0.60 V vs. RHE, which is outstanding among the metal oxide-based catalysts for 2e-ORR. Such performance is closely associated with the mesoporous structures of the carbon nanosheets. Furthermore, the appropriate bonding strength of Ni-OH derived from the amorphous nature is crucial for the high selectivity. The theoretical calculation reveals that the *OOH intermediate prefers to adsorb on the amorphous NiO_x-C by the end-on mode, facilitating the 2e-ORR process. The present amorphous NiO_x loaded on carbon nanosheets can be promising electrocatalysts for synthesizing H₂O₂ after the stability issues are well addressed.

1. INTRODUCTION

H₂O₂, as a multifunctional and environmentally friendly oxidant, is a very important chemical in modern industry, which has wide applications in bleaching, textile industry, chemical synthesis, waste water treatment, disinfection, semiconductor manufacturing.^{1,2} Currently, ~95% of H₂O₂ is synthesized by the anthraquinone process, which is, however, energy-intensive, time-consuming and also produces many by-products. In addition, the storage and transportation of highly concentrated H₂O₂ produced from the anthraquinone process also poses serious safety risks. In such context, the two-electron reduction of O₂ is attracting increasing attention due to its environmental friendliness and on-site production of dilute H₂O₂.

The electrochemical oxygen reduction reaction (ORR) is a multi-electron reaction, which can proceed via the four-electron route to form H₂O ($O_2 + 2H_2O + 4e^- \rightarrow 4OH^-$ in basic medium) or via the two-electron route to form H₂O₂ ($O_2 + H_2O + 2e^- \rightarrow HO_2^- + OH^-$ in basic medium). The reaction mechanisms of both routes have been widely studied,^{3,4} which involve the same first intermediate of *OOH. Whether the product is H₂O or H₂O₂ depends on the tendency to break the O-O bond.^{1,2} The further single-electron reduc-

tion of *OOH results in the selective production of H₂O₂, but the further reduction to H₂O is inhibited only on catalysts that can maintain the O-O bond. Therefore, the rational design of catalysts with appropriate bonding strength with *OOH is the key to achieve efficient and selective two-electron reduction of O₂.^{5,6}

Various electrocatalysts towards 2e-ORR have been developed. Noble metals such as Au clusters,⁷ Pt/TiN,⁸ or metal alloys such as Au-Pd,⁹ Pt-Hg,⁵ Au-Pt-Ni¹⁰ are effective to promote the 2e-ORR. However, the large-scale application of noble metal catalysts is limited by their high cost and earth-scarcity. In contrast, the non-noble metal (e.g., Ni, Co, Fe)-based materials¹¹⁻¹³ and carbon-based materials^{1,14} are promising alternatives. In particular, the reasonable modification can greatly improve the catalytic performance of non-noble metal oxides, even comparable to the noble metal catalysts.¹⁵⁻¹⁹ Since the electrical conductivity of many metal oxides (except IrO₂, RuO_x, etc) is generally not high enough for electrocatalysis, they are supported on conductive supports such as the carbon-based materials. The pore characteristics, the defect structure, and the heteroatom doping^{1,20} provide great opportunities to tune the ORR properties. It is widely proved that carbon that has high proportion of mesopores shows higher activi-

ty towards 2e-ORR because such microstructure is beneficial for mass transfer, favoring the releasing of generated H_2O_2 and avoiding the further reduction to H_2O and thus leading to high selectivity to H_2O_2 .^{21,22}

The amorphous metal oxides show much higher electrocatalytic activity than their crystalline counterparts towards oxygen evolution reaction,²³⁻²⁵ urea oxidation reaction²⁶ at the potentials when the electrical conductivity of materials is not dominating, due to their more coordinately unsaturated cation sites available for reaction, the isotropic and single-phase characteristics.²⁷ Although there are very limited studies on the amorphous metal oxides as catalysts for 2e-ORR, the traces demonstrate that the amorphous materials can be competitive catalysts. The sub-5 nm amorphous Pd nanoparticles prepared by the electrochemical deposition from Pd ions during O_2 reduction yields H_2O_2 selectivity of > 95% and high kinetic current density.²⁸ The semiconducting metal-organic graphene analog $\text{Ni}_3(\text{HITP})_2$ with low crystallinity shows high selectivity of 80% towards 2e-ORR over 0.2-0.6 V vs. reversible hydrogen electrode (RHE) in 0.1 M KOH.²⁹ The coordinatively unsaturated nature of the central Ni atoms in metal-organic framework has more open sites for the adsorption of oxygen molecules and thus is preferred for H_2O_2 synthesis.¹⁵ The hydrogen plasma etched TiO_{2-x} with poor crystallinity at the surface shows high 2e-ORR performance.³⁰ Very recently, the amorphous NiO nanosheets is found to be effective towards H_2O_2 production compared with its crystalline counterpart, with selectivity of 88.9-90.4% vs. 28.4-34.7% at potential of 0.2-0.6 V vs. RHE in 0.1 M KOH.³¹

Herein, the amorphous nickel oxides, prepared by a simple and scalable method, were designed as electrocatalysts for 2e-ORR. The results show that in 0.1 M KOH, the amorphous NiO_x supported on carbon nanosheets show higher activity and selectivity (~91%) over a wide potential range of 0.15-0.60 V vs. RHE towards 2e-ORR compared with the crystalline NiO.

2. EXPERIMENTAL

2.1. Catalyst synthesis

The carbon nanosheets (C) were prepared by pyrolysis of sodium citrate (Tianjin Yuanli Co., Ltd, GR) at 650-800 °C for 1 h in Ar atmosphere³². The resultant powders were washed with 0.5 M H_2SO_4 to remove the inorganic impurities and then with the deionized water until it is neutral, followed by vacuum drying at 60 °C for 24 h.

The NiO_x -C catalysts were synthesized by the photochemical metal organic deposition (PMOD) method, which is a classical method to prepare amorphous materials.^{23-25, 33, 34} Briefly, the nickel (II) 2-ethylhexanoate (78% in 2-ethylhexanoic acid, Strem, 10-15% Ni) precursor was dissolved in a mixed solution of n-hexane (Tianjin Yuanli Co., Ltd, AR) and acetone (Tianjin Damao Co., Ltd, AR). Then required amount of carbon was added. The mixture was ultrasonicated for 30 min, during which the temperature was controlled < 30 °C by adding ice from time to time. Subsequently, the mixture was magnetically stirred in a fume hood to volatilize the solvent. The resultant concen-

trated dispersion was evenly coated on an aluminum foil, followed by being irradiated with ultraviolet light (185 and 254 nm) for 12 h to form the composite NiO_x -C. In the composite, the Ni content (mass ratio of Ni to Ni+C) was varied over 5-40%. The obtained NiO_x -C was then subjected to heat treatment at 200, 400, and 600 °C for 1 h in flowing Ar (100 ml min^{-1}) in a tube furnace at a heating rate of $5 \text{ }^\circ\text{C min}^{-1}$.

2.2. Characterization

Fourier transform infrared (FTIR) spectroscopy (Nicolet 6700 model) was used to monitor the decomposition process of metal organic precursor. The phase evolution was examined by X-ray diffraction (XRD, Rigaku Corporation D/MAX-2500 diffractometer) with $\text{Cu K}\alpha$ radiation. X-ray photoelectron spectroscopy (XPS, Thermo Fisher Scientific Escalab-250Xi) was conducted on a SPECS system with Al $\text{K}\alpha$ as the X-ray source. The binding energy was calibrated with adventitious C 1s at 284.8 eV. The morphologies were observed by scanning electron microscopy (SEM, FEI Company Apreo S LoVac microscope) equipped with an energy dispersive spectrometer (EDS) unit. The nitrogen sorption isotherms analysis was performed on physical sorption instrument (Quantachrome Autosorb-1) in liquid nitrogen at -196 °C. The uncalcined and 200 °C-calcined samples were degassed at 150 °C for 6 h whereas those calcined at 400 and 600 °C were degassed at 300 °C for 6 h. The surface area of micropore was estimated using the t-plot method. The pore size distribution (PSD) was obtained by non-linear density functional theory (NLDFT) method.

2.3. Electrochemical test

The catalyst inks were prepared by mixing NiO_x -C (2 mg), C (0.5 mg) with isopropanol (Tianjin Yuanli Co., Ltd, AR, 250 μL), deionized water (250 μL) and Nafion (D-520, 5%, 10 μL) and then ultrasonicated for 30 min. 12.5 μL of ink was pipetted onto the glassy carbon disk and left to dry for 2 h at room temperature, followed by adding 4 μL of Nafion alcohol solution (0.5 wt.%). The ORR performance was evaluated with rotating ring-disk electrode (RRDE, Pine Electronic, America, E7R9, $d = 5.61 \text{ mm}$) controlled by the electrochemical station (CHI 760E) in a three-electrode setup in 0.1 M KOH, where the RRDE, Pt mesh and Hg/HgO were used as the working, counter and reference electrodes, respectively. RRDE was polished with 50 nm alumina slurry for at least 5 min before use.

The electrochemical test was first performed in N_2 atmosphere. Cyclic voltammetry (CV) was scanned between -0.9 and 0.2 V vs Hg/HgO at 200 mV s^{-1} for 50 cycles to obtain a steady state. Next, CV was scanned at 20 mV s^{-1} for 2 cycles and linear sweep voltammetry (LSV) at 10 mV s^{-1} with 1600 rpm. Subsequently the electrolyte was purged with O_2 for 30 min. CV and LSV were then recorded. During the LSV test, the Pt ring potential was held at 0.6 V vs Hg/HgO . All the ORR polarization current was corrected by subtracting the capacitive background current. The electrochemical double-layer capacitance (C_{dl}) of the catalysts was determined from CV in the non-Faradaic reaction region (0-0.1 V vs. Hg/HgO) at different scan rates ($10\text{-}70 \text{ mV s}^{-1}$). The electron transfer number (n) and HO_2^- selec-

tivity (%) were calculated according to eqs. 1 and 2, respectively.

$$n = 4 * \frac{I_{\text{ring}}}{|I_{\text{disk}}| + I_{\text{ring}}/N} \quad (1)$$

$$\text{HO}_2^- \text{ selectivity (\%)} = 200 * \frac{I_{\text{ring}}/N}{|I_{\text{disk}}| + I_{\text{ring}}/N} \quad (2)$$

where I_{disk} and I_{ring} are the disk and ring currents, respectively. N is the collection efficiency, which is determined by the size of RRDE and here is 0.37.

The mass-transport-corrected kinetic partial current density (J_k) for H_2O_2 production was calculated according to eq.3.

$$\frac{1}{J} = \frac{1}{J_d} + \frac{1}{J_k} \quad (3)$$

where J is the total current, J_d is the mass-transport-limited current to H_2O_2 production (obtained from the ring).

The durability of catalysts was examined by accelerated durability test (ADT) via 10000 CV cycles. All the potentials were converted to RHE.

2.4. First-principles calculations

All calculations were performed using first-principles density functional theory (DFT), as executed in the Vienna Ab initio Simulation Package (VASP).^{35,36} The exchange correlation functional employed was the Perdew-Burke-Ernzerhof (PBE) functional of generalized gradient approximation (GGA).³⁷ The simulation of aqueous solution environment relies on the combination of implicit solvent model (VASP Solvation Package).^{38,39} Each free energy was corrected by vibrational frequency analysis, which was thermodynamically corrected at room temperature of 293.15 K. A plane-wave cut-off of 520 eV was applied to expand the electron wave functions and the core electrons were replaced by the projector augmented wave (PAW) pseudopotentials. A sufficient vacuum layer (20 Å) was added to the z-axis to eliminate all hypothetical interactions between metal surfaces. The reciprocal space was sampled using a $3 \times 3 \times 1$ mesh grid by using the Gamma k-point scheme. The structures were relaxed until the total energy variation was less than 10^{-7} eV and all forces on each atom were less than 0.01 eV \AA^{-1} . The DFT-D3 approach was used to describe the van der Waals interactions.⁴⁰ The crystalline NiO_x surfaces were simulated using slabs containing 4-layer and the 2-layer terminations, respectively. The original model of amorphous $\text{NiO}_x\text{-C}$ was obtained through thermostatic molecular dynamics simulation, and a double-layer C-periodic structure was used to simulate the carbon carrier. A typical method for calculating the Gibbs free energy is according to eqs. 4 and 5.

$$\Delta E_{\text{ads}} = E_{\text{total}} - (E_{\text{adsorbate}} + E_{\text{surface}}) \quad (4)$$

$$\Delta G = \Delta E_{\text{ads}} + \Delta E_{\text{sol}} + \Delta ZPE - T\Delta S - neU \quad (5)$$

where E_{total} is the total energy of the adsorbed surface. $E_{\text{adsorbate}}$ is the energy of the adsorbed surface. E_{surface} is the energy of the pure surface. ΔG is the Gibbs free energy of

each ORR process. ΔE_{sol} , ΔZPE , T , ΔS and neU are the solvation correction energy, zero-point energy, temperature, entropy and the relative equilibrium potential, respectively. By empirical definition, the negative value of E_{ads} represents the energy released or relatively stable adsorption.

3. RESULTS AND DISCUSSION

The amorphous NiO_x was prepared by the PMOD method,^{23-25,33,34} where the organic ligands C-H ($3000\text{-}2800 \text{ cm}^{-1}$) and C=O ($1700\text{-}1400 \text{ cm}^{-1}$, Figure S1) decompose into CO_2 and H_2O during UV irradiation, accompanied by the electron transfer from ligands to metal center. The metal is oxidized in the ambient air atmosphere.³³ Based on the FTIR result, the photolysis is complete within 12 h. The XRD results of $\text{NiO}_x\text{-C}$ calcined at different temperatures are shown in Figure 1. Only a broad and weak diffraction peak at 23° is observed for C due to its low graphitization degree. No obvious difference is found for the uncalcined and 200°C -calcined $\text{NiO}_x\text{-C}$ samples compared with C, indicating their amorphous nature, which has been widely confirmed.^{23,33,34} With temperature increasing to 400°C , however, NiO appears, which indicates the occurrence of crystallization at temperatures $\geq 400^\circ\text{C}$. The diffraction intensity increases further when the calcination temperature elevates to 600°C , along with the appearance of Ni metal due to the reduction of NiO_x by carbon in the compo-

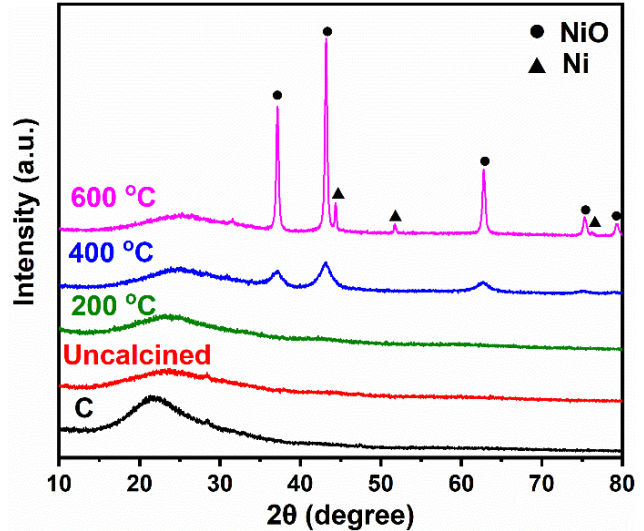


Figure 1. XRD patterns of pristine carbon nanosheets pyrolyzed at 800°C and $\text{NiO}_x\text{-C}$ calcined at different temperatures.

To further examine the oxidation state of elements at the surface, XPS was run. For the uncalcined and 200°C -calcined catalyst, Ni exists as mainly Ni^{2+} (Figure 2a) with the binding energy at $\sim 856.5/874.2 \text{ eV}$.²⁹ When the

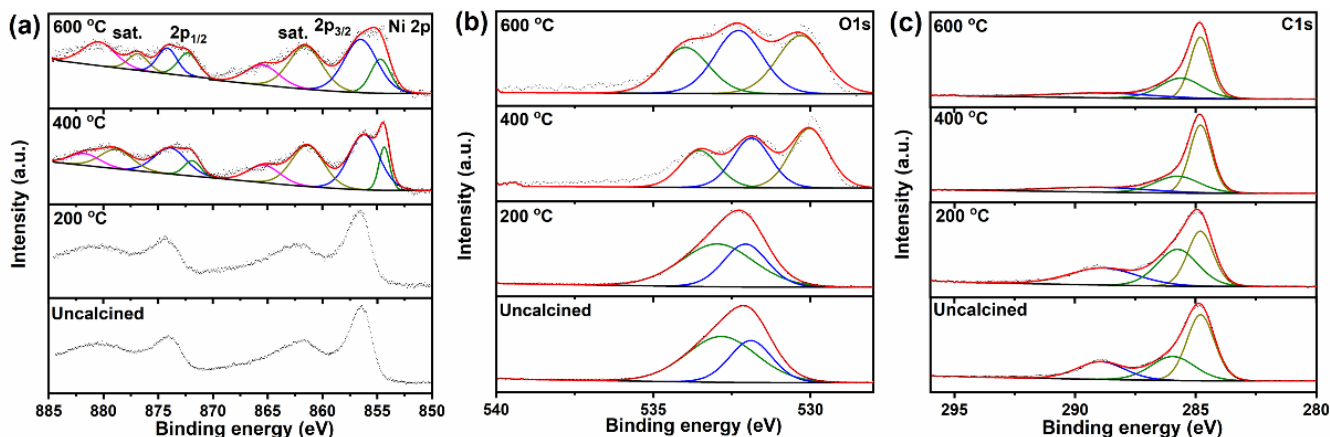


Figure 2. XPS spectra of Ni 2p, O 1s and C 1s for NiO_x-C calcined at different temperatures. (a) Ni 2p. (b) O 1s. (c) C 1s.

calcination temperature increases to 400 and 600 °C, peaks at ~854.3/871.9 eV appear, indicating the formation of Ni metal due to the reduction of NiO_x by carbon in the composite catalysts. The O 1s spectra (Figure 2b) can be deconvoluted into lattice oxygen at ~530.0 eV, epoxy/hydroxyl (C-O) at ~532.0 eV, carbonyls (C=O) at 533-534 eV.⁴¹ Similarly, the deconvolution of C 1s spectra (Figure 2c) shows several peaks, sp² bonded carbon at 284.8 eV, carbon singly bound to oxygen (C-O) at 285.8 eV, carbon bound to two oxygen (COOH) at ~289.0 eV.¹⁴ For the uncalcined and 200 °C-calcined samples, C-O and COOH bonds dominate, which have been widely reported as the active sites for 2e-ORR.^{14, 41, 42} As the calcination temperature increases, the lattice oxygen appears at ≥ 400 °C, also an indicator of the crystallization. The characteristic peaks (C=O) exhibit obvious shift to higher binding energy with the calcination temperature, which may result from the formation of carbon vacancies.^{14, 42}

In this work, the carbon nanosheets were prepared from pyrolysis of sodium citrate considering its high mesoporosity,³² which is reported to be beneficial for the 2e-ORR process.^{21, 22} The microstructures of pristine carbon pyrolyzed at different temperatures were examined by SEM and N₂ sorption (Figures 3a and S2). All the carbon materials have a three-dimensional honeycomb shape assembled with carbon nanosheets, forming large number of μm-scale pores, similar with the reported.³² Furthermore, each carbon sheet contains cracks of mesopores and micropores. The Brunauer-Emmett-Teller surface area (S_{BET}) of pristine carbon increases with the pyrolysis temperature from 650 to 750 °C, but further increasing the temperature results in declined surface area probably due to the growth of micropores, as evidenced by the increased proportion of mesopore surface area (S_{meso}, Table S1). After loading NiO_x on the 800 °C-pyrolyzed carbon sheets by the PMOD process, the porosity decreases obviously, with NiO_x infiltrating into the pores (Figure 3b). Nevertheless, the mesopores and micropores still exist in each carbon sheet. Such hierarchical microstructure can provide more active sites

and mass transfer channels, which facilitates the catalytic process.⁴³ The elemental mapping (Figure S3) reveals that Ni distributes uniformly in the porous carbon. The calcination temperature has a significant impact on the microstructure (Figure S4). The 200 °C-calcined samples show similar microstructure with the uncalcined ones. However, the 400 °C treatment results in the partial collapse of the hierarchical microstructure and the carbon sheets tend to aggregate. The 600 °C treatment leads to complete damage to the structure. No 3D honeycomb structure can be found; instead, the samples are composed of nanoparticles although they are still porous.

The pore properties of NiO_x-C calcined at different temperatures were further examined by N₂ sorption and the results are shown in Figures 3c and d. All the isotherm curves exhibit a hysteresis loop at medium to high relative pressure, indicating the presence of mesopore and macropore. In addition, the type I isotherms are also observed indicating the existence of micropore, which is further confirmed by the PSD results. The results clearly demonstrate the hierarchically porous structure. The detailed pore properties are listed in Table 1. Loading NiO_x seriously reduces S_{BET} of carbon from 473.4 to 141.6 m² g⁻¹, both micropore and mesopore. Accordingly, the Ni-precursors preferably enter the micropores due to the large capillary force and also occlude the mesopores. However, the proportion of mesopores increases from ~60% to 94%. Although the 200 °C calcination shows no influence on S_{BET}, the micropore surface area (S_{micro}) increases probably due to the elimination of adsorbed surface functional groups. Further increase in the baking temperature results in increase in all the surface area, but the proportion of mesopore decreases. During heat-treatment in Ar atmosphere, NiO_x can be reduced to Ni metal by carbon in the composite, leading to generation of micropore and thus quickly increased S_{micro}. However, the 600 °C-calcination is high enough to induce the sintering of NiO_x and Ni particles, growth and even collapse of the mesopores, leading to reduced S_{BET} and mesopore proportion.

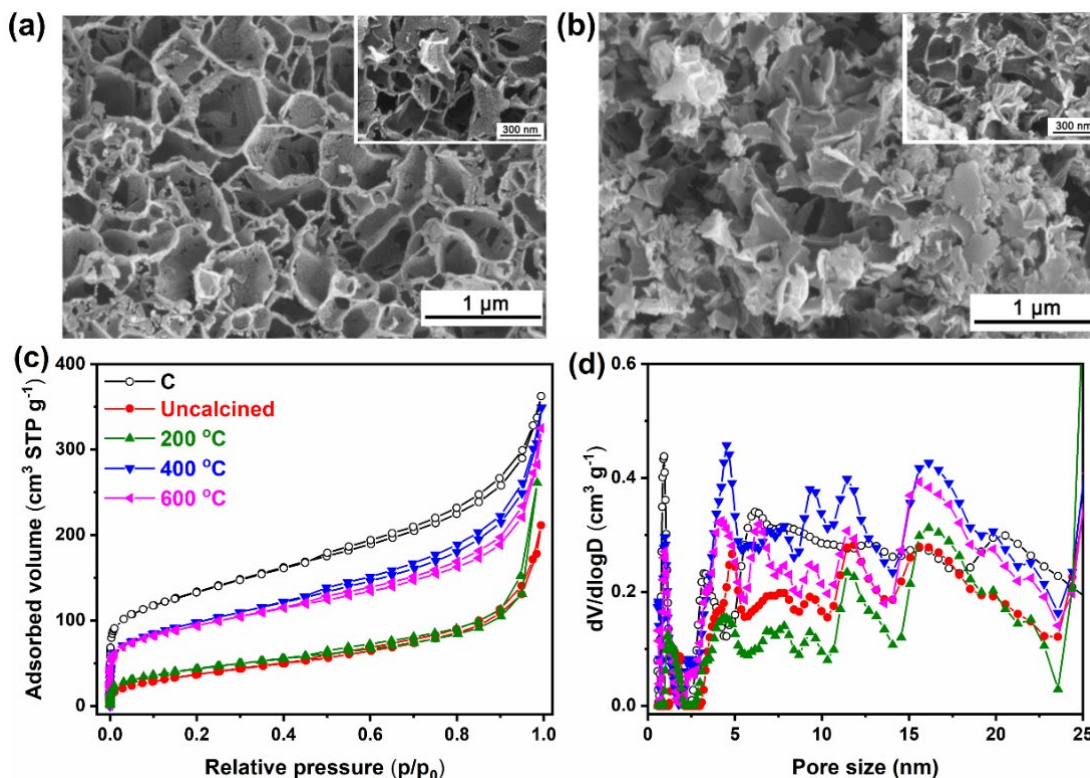


Figure 3. (a) SEM images of pristine carbon nanosheets pyrolyzed at 800 °C. (b) SEM images of NiO_x-C. (c) Nitrogen sorption isotherms and (d) Pore size distribution (PSD) of C and NiO_x-C calcined at different temperatures.

Table 1 Pore properties of pristine carbon nanosheets pyrolyzed at 800 °C and NiO_x-C calcined at different temperatures.

Sample	Surface area (m ² g ⁻¹)			S _{meso} /S _{BET}
	S _{BET}	S _{micro}	S _{meso}	
C	473.4	190.3	283.1	0.598
Uncalcined	141.6	8.1	133.5	0.943
200 °C	155.8	39.1	116.7	0.750
400 °C	344.8	111.4	237.4	0.688
600 °C	333.6	148.3	185.4	0.556

As aforementioned, the pore property has a significant influence on the 2e-ORR. During our initial screening, we loaded 20% Ni on the carbon sheets pyrolyzed at 650-800 °C and tested the ORR performance. The CV results in N₂-saturated and O₂-saturated 0.1 M KOH are shown in Figure S5a. No visible oxygen reduction peaks in N₂-saturated KOH can be found, which implies that no reduction reaction occurs in nitrogen atmosphere. However, in O₂-saturated KOH, there are distinctive oxygen reduction peaks, indicating that these catalysts could catalyze the ORR in the oxygen atmosphere. The LSV curves in O₂-saturated KOH are shown in Figure S5b. The disk current maintains almost constant with the pyrolysis temperature, however, the ring current increases, being maximum for the 800 °C-pyrolyzed samples. All the samples show high 2e selectivity (Figure S5c), with the HO₂⁻ selectivity > 70% and electron transfer number < 2.6. In particular, the 800 °C-related samples show the highest HO₂⁻ selectivity and

lowest n over a wide potential range. In addition, the loading amount of Ni also has an impact on the catalytic performance and 20% is the optimum value (Figure S6). Accordingly, the NiO_x-C composite with 20% Ni loaded on 800 °C-pyrolyzed carbon nanosheets were selected for further study.

Before further discussion, the role of glassy carbon electrode should be noted. It is well-known that the glassy carbon is active for 2e-ORR in alkaline solution.^{3, 17, 44, 45} In our work, the NiO_x-C catalysts were loaded onto the glassy carbon. The ORR performance of pristine glassy carbon in 0.1 M KOH was tested and the results are shown in Fig. S7. It shows superior selectivity towards 2e-ORR, with ~98% selectivity over a wide potential range (0.5-0.1 V vs. RHE), which is similar with the reported.^{3, 17, 44, 45} However, the activity is rather poor, with onset potential at 0.58 V vs. RHE. When the amorphous NiO_x-C was loaded, the 2e-ORR activity is substantially increased, with the ring current increasing and the onset potential shifting to more positive potential although the selectivity decreasing slightly. Such results reveal that it is the NiO_x-C loaded on glassy carbon that determines the activity, rather than the glassy carbon. It is probably due to the fact that the NiO_x-C ink was evenly coated and formed a uniform film on the glassy carbon, preventing the exposure of glassy carbon to the electrolyte solution.

To investigate the effect of crystallization on the 2e-ORR performance, the corresponding LSV results in O₂-

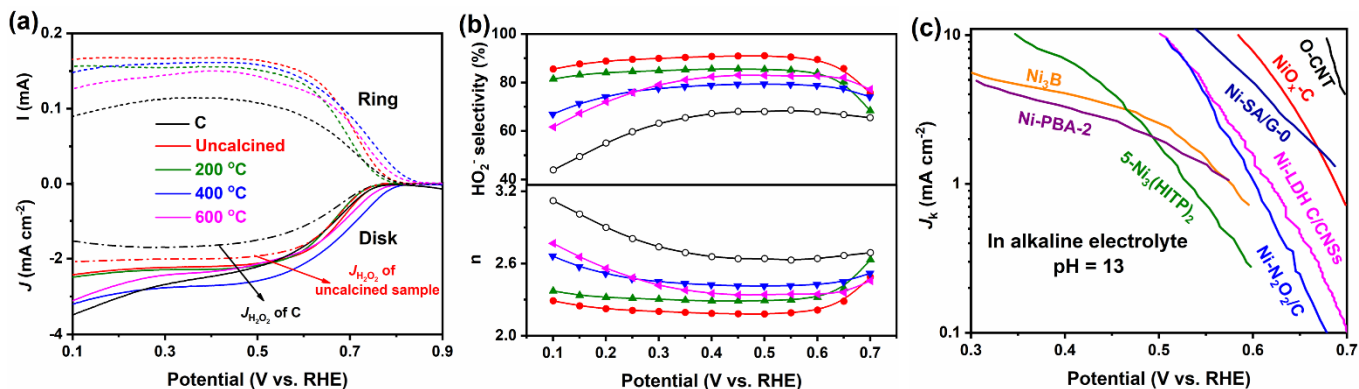


Figure 4. Catalytic performance of C, NiO_x-C calcined at different temperatures. (a) LSV curves of C, NiO_x-C calcined at different temperatures at a scan rate of 10 mV s⁻¹, 1600 rpm in O₂-saturated 0.1 M KOH. The H₂O₂ partial current density ($J_{H_2O_2}$) of uncalcined NiO_x-C and pristine carbon was also included. (b) Electron transfer number (n) and HO₂⁻ selectivity (%). (c) Comparison of mass-transport-corrected kinetic partial current density for H₂O₂ production.

saturated 0.1 M KOH are shown in Figure 4a. The pristine carbon was also included for comparison. The pristine porous carbon shows high disk current, which is highest at the most negative potential, which is probably due to its high mesoporosity and high content of oxygen defects.^{1, 14, 46} However, it shows only moderate ring current, $J_{H_2O_2}$ and onset potential (0.76 V vs. RHE). After loading amorphous NiO_x, the disk current decreases whereas the $J_{H_2O_2}$ increases, by 30%, 17% and 18% at 0.6, 0.4 and 0.2 V, respectively, indicating the increased 2e-ORR activity and selectivity. This result infers that carbon and amorphous NiO_x are essential for high activity and selectivity towards 2e-ORR. The 200 °C-calcined sample shows no obvious difference in disk current but lower ring current compared with the uncalcined one. However, the 400 and 600 °C-calcination leads to enhanced disk current along with positive shift in onset potential (0.80 and 0.78 V for 400 and 600 °C samples, respectively) but decreased ring current, indicating decreased 2e-ORR activity and selectivity, which is proved by the decreased HO₂⁻ selectivity and increased n values (Figure 4b). The uncalcined samples show almost constant HO₂⁻ selectivity of 91% and n values of 2.2 over a wide potential range of 0.15-0.60 V vs. RHE, but the 400 and 600 °C samples show quickly decreased HO₂⁻ selectivity and increased n value when the potential is lower than 0.3 V. The HO₂⁻ selectivity is 85.4%, 79.4% and 82.9% at 0.5 V, 84.0%, 74.1% and 72.0% at 0.2 V for the 200, 400 and 600 °C-calcined samples, respectively. The results apparently reveal that the amorphous NiO_x loaded on carbon nanosheets shows higher 2e-ORR activity and selectivity (onset potential of 0.76 V vs. RHE, HO₂⁻ selectivity of ~91%) than its crystalline counterpart, which are also higher than the reported metal oxides such as Nb₂O₅-rGO (0.76 V, 74.9%),¹⁶ Fe₃O₄/graphene (0.79 V, 62%),¹⁷ Co_xO_y/C (0.69 V, 74%)¹⁸ and 4% CeO₂/C (0.75 V, 88%).¹⁹ Furthermore, the performance of the present amorphous NiO_x-C is comparable with the reported amorphous materials such as MOF NSs-300 (0.75 V, 99%),¹⁵ Pd (0.65 V, 95%)²⁸ and 5-Ni₃(HITP)₂ (0.69 V, 80%),²⁹ a-NiO NSs (0.74 V, 90.4%).³¹ The detailed comparison can be found in Table S2.

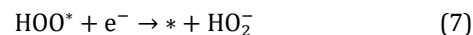
The mass-transport-corrected kinetic partial current density for H₂O₂ production (j_k), which is a common metric for 2e-ORR,^{3, 5} is presented in Figure 4c for our amorphous NiO_x-C and the reported catalysts.^{14, 29, 41, 47-50} Obviously, the amorphous NiO_x-C shows outstanding performance. Considering the easy fabrication and excellent performance, the amorphous NiO_x supported on carbon nanosheets can be promising catalyst for H₂O₂ production.

To gain an in-depth understanding of the better 2e-ORR performance of the amorphous materials, the electrical double layer capacitance (C_{dl}) was measured, which is an evaluation of the electrochemical surface area. It should be noted that C_{dl} has limitation in interpreting the active surface area for electrocatalysis.⁵¹ Here we use C_{dl} to qualitatively illustrate the change trend of surface area of samples calcined at different temperatures. C_{dl} is measured by CV in the non-Faradaic potential range with various scan rates and the results are shown in Figure 5a. C_{dl} shows similar trend with S_{BET} . Interesting, C_{dl} shows good correlation with the disk current in Figure 4a, but it cannot explain the 2e-ORR selectivity. During the 2e-ORR process, the O₂ molecules combine with electrons to generate H₂O₂, which is released from the pores or continues to react to generate H₂O. Therefore, the larger pores such as mesopores facilitate the overflow of the generated H₂O₂ from the pores.^{43, 52, 53} As shown in Figure 5b, the 2e-ORR selectivity is almost linearly related with the proportion of mesopores (S_{meso}/S_{BET}), showing the strong dependence of 2e-ORR selectivity on the pore properties.

In alkaline medium, 2e-ORR proceeds with eq. 6,



followed by eq. 7.



where * is the active site.¹³ The catalytic activity and selectivity are determined by the binding strength of the reaction intermediate *OOH with the active site, here we assume the Ni-related species. Considering the constant scaling between the binding free energy of *OOH and *OH of ~3.29 eV,⁵⁴ the binding free energy of HO* is used as a de-

descriptor for the current 2e-ORR. The metal-OH binding energy was calculated with eq. 8.^{55,56}

$$D(M-OH) = 38.96 - \Delta H_{M_yO_x}^0/2x + 23.06(X_M - X_{OH})^2 \quad (8)$$

where $\Delta H_{M_yO_x}^0$ is the negative heat of formation of the oxide M_yO_x at 298 K; X_M is the electronegativity of metal element and X_{OH} is 3.3.²⁵

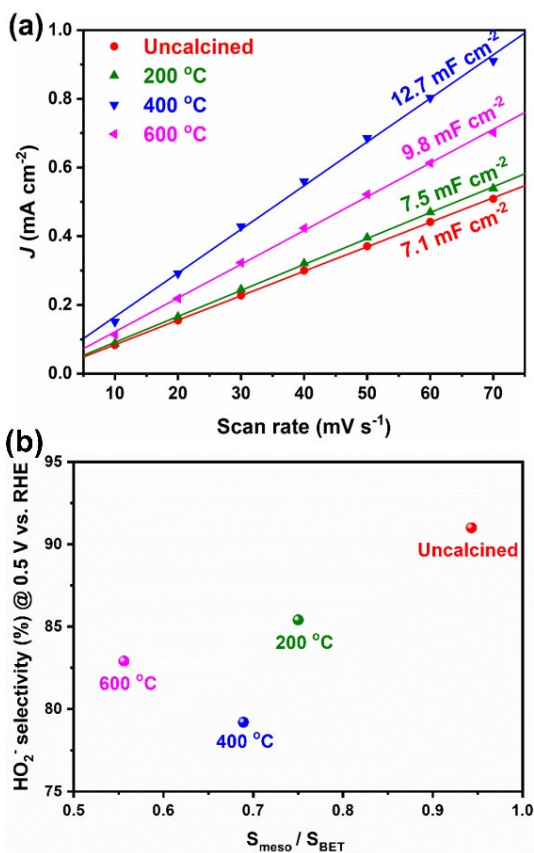


Figure 5. (a) Double-layer capacitance of NiO_x-C calcined at different temperatures. (b) Relationship between HO₂⁻ selectivity and S_{meso}/S_{BET} for NiO_x-C calcined at different temperatures.

The relationship between M-OH bond strength and 2e selectivity is illustrated in Figure 6 and Table S3; the detailed LSV, HO₂⁻ selectivity and n values are provided in Figure S8. It is obvious that NiO_x shows the highest selectivity, probably due to its appropriate M-OH bonding strength, which is critical for the 2e-ORR route.¹ It is noted that the bond strength here is calculated based on the crystalline materials. It can be smaller due to the amorphous nature where the local coordination environments distribute in a disordered range.⁵⁷ In addition, compared with the crystalline NiO_x in this work and the reported,^{15,28,29} the present amorphous NiO_x supported on carbon nanosheets shows outstanding 2e-ORR activity and selectivity, which is probably originated from its amorphous nature. The ORR mechanism depends on the way O₂ interacts with the catalyst surface. Among the three models, the Pauling model is desirable for the 2e-ORR, where the oxygen molecule interacts in an end-on position with no rupture of the O-O bond and thus generating H₂O₂.⁵⁸ It is reported that

the coordination number (CN) significantly affect the adsorption model. The lower the CN, the higher selectivity towards 2e-ORR.^{15,28,59} The amorphous material is characterized by abundant unsaturated sites and isotropic nature,^{23,25} which is probably beneficial for the adsorption of O₂ molecule according to the Pauling model. Such argument is also proved by the recent report.³¹

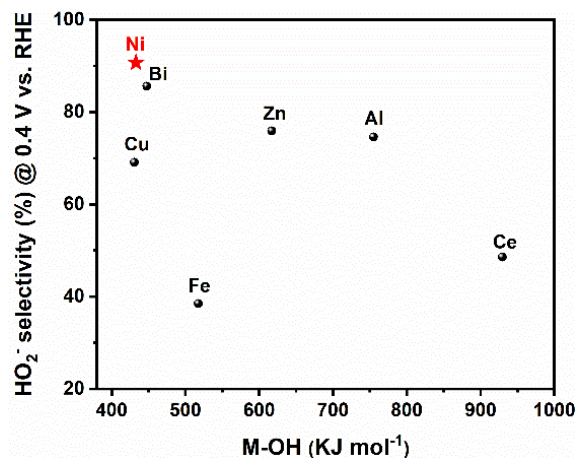


Figure 6. Relationship between M-OH bond strength and the selectivity towards 2e-ORR.

The theoretical Tafel slope for eqs. 6 and 7 are 120 and 40 mV dec⁻¹, respectively. The Tafel slope is 79.1, 66.4, 62.2, 122.8 and 96.9 mV dec⁻¹ for C, uncalcined, 200-, 400- and 600 °C-treated catalysts, respectively (Figure S9a). The corresponding results for the MO_x-C catalysts are provided in Figure S9b and Table S3 with 50-85 mV dec⁻¹. Accordingly, the first step of forming *OOH (eq.6) is the dominated rate-determining step (RDS) for the 400- and 600 °C-calcined samples, whereas probably the second step (eq. 7) for the amorphous samples during 2e-ORR, which is also proved by the theoretical calculation results below. In addition, according to Holewinski and Linic, the Tafel slope decreases with the coverage of OH (θ) from 120 to 60 mV dec⁻¹ when θ increases from 0 to 0.6.⁶⁰ Generally, the amorphous materials show more unsaturated sites at the surface and thus higher coverage,^{25,61} which is beneficial for the adsorption of reactants. Accordingly, the supported amorphous NiO_x samples show the lowest Tafel slope, indicating the fastest reaction kinetic process.

To further explore the 2e-ORR process, the DFT calculation was performed. Here, the implicit solvent model is used to compare and correct the thermodynamic properties of crystalline NiO_x and amorphous NiO_x-C during ORR. For the adsorption pattern, *OOH tends to adsorb on the crystalline NiO_x by the side-on mode, with O-O bond significantly being elongated to ~1.40 Å (compared with the original length of 1.25 Å), leading to the breakage of O-O bond and thus forming Ni-O and Ni-OH structure (Figure 7a), which is beneficial for the 4e-ORR process. However, *OOH prefers to adsorb on the amorphous NiO_x-C by the end-on mode, with O-O bond slightly being elongated to ~1.30 Å, forming Ni-O-OH, which greatly facilitates the 2e-ORR to form H₂O₂ (Figure 7b).^{58,62,63} The free energy dependent reaction coordinate diagram was calculated and is

shown in Figure 7c and d. For 2e-ORR, the amorphous NiO_x has a lower overpotential than crystalline NiO_x , with theoretical overpotential of 0.45 and 2.58 V, respectively. Furthermore, they show different RDS, which is from $^*\text{OOH}$ to HO_2^- for amorphous $\text{NiO}_x\text{-C}$ but from O_2 to $^*\text{OOH}$ for crystalline NiO_x (Figure 7c), which is in agreement with the change of Tafel slope as aforementioned. For 4e-ORR, the RDS is from $^*\text{OOH}$ to $^*\text{O}$ (theoretical overpotential: 1.86 V) for amorphous $\text{NiO}_x\text{-C}$ but O_2 protonation (theoretical overpotential: 2.32 V) for crystalline NiO_x (Figure 7d). The amorphous material still has obvious thermodynamic superiority. By comparing Figure 7c and d, the amorphous $\text{NiO}_x\text{-C}$ prefers to generate HO_2^- at lower overpotential through the 2e process, leading to the higher activity and selectivity towards 2e-ORR.

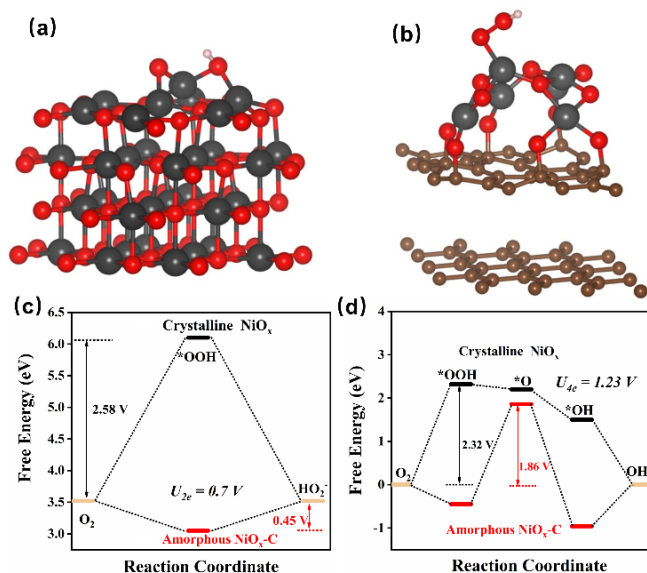


Figure 7. Adsorption model of $^*\text{OOH}$ on (a) crystalline NiO_x and (b) amorphous $\text{NiO}_x\text{-C}$. The black, red, brown and pink balls are Ni, O, C and H atoms, respectively. The reaction coordinate of amorphous $\text{NiO}_x\text{-C}$ and crystalline NiO_x for (c) 2e-ORR and (d) 4e-ORR transport processes in alkaline solution.

The durability is an important performance matrix of the catalyst, which is evaluated by ADT. As shown in Figure 8a, both the disk current and the ring current decrease slightly, the half-wave potential was shifted negatively by 20 mV. In addition, the 2e-ORR selectivity changes slightly. The postmortem SEM analysis (Figure 8b) reveals that microstructure was damaged to some extent, which should be responsible for the performance degradation. The degradation of amorphous materials during electrocatalysis has been widely reported,^{24, 28, 34} which are believed to be related with the leaching of active species into the solution. Improving the interaction between the active species with the support can be an alternative to improve the stability.^{11, 28}

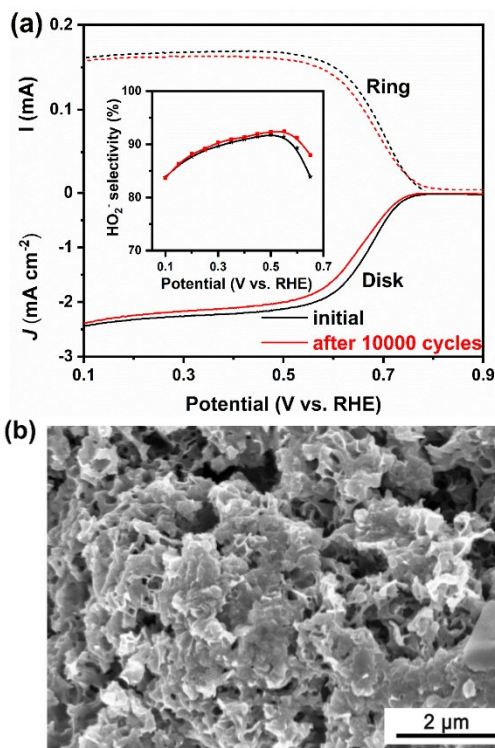


Figure 8. Durability test of $\text{NiO}_x\text{-C}$ catalyst to produce H_2O_2 . (a) Catalytic performance of $\text{NiO}_x\text{-C}$ catalyst before and after durability test. (b) SEM microstructure after durability test.

4. CONCLUSIONS

This work demonstrates that the amorphous NiO_x prepared by the facile PMOD method onto the carbon nanosheets can be highly active and selective towards 2e-ORR to produce H_2O_2 . The hierarchical property of the carbon support is critical for the high performance. Both amorphous NiO_x and the mesoporous carbon nanosheets are essential for the high performance, contributing to the high onset potential of 0.76 V vs. RHE and high HO_2^- selectivity of $\sim 91\%$ and n of ~ 2.2 over 0.15-0.60 V vs. RHE, which is superior to its crystalline counterparts and higher than that of most reported 2e-ORR electrocatalysts. The amorphous nature renders the preferential end-on adsorption of $^*\text{OOH}$ on the active sites and the appropriate Ni-OH bond strength affords high selectivity towards H_2O_2 formation. This work sheds lights on the development of high-performance and cost-effective 2e-ORR electrocatalysts by engineering the crystallinity of metal oxides and the pore structure of the carbon support.

ASSOCIATED CONTENT

AUTHOR INFORMATION

Corresponding Authors

Ji-Jun Zou - School of Chemical Engineering and Technology, Tianjin University, Tianjin 300072, China; Collaborative Innovation Center of Chemical Science and Engineering (Tianjin), Tianjin 300072, China. Email: jj_zou@tju.edu.cn

Cuijuan Zhang - State Key Laboratory of Chemical Engineering, Tianjin Key Laboratory of Applied Catalysis, Science and Technology, School of Chemical Engineering and Technology, Tianjin University, Tianjin 300072, China; Collaborative Innovation Center of Chemical Science and Engineering (Tianjin), Tianjin 300072, China. Email: cjzhang@tju.edu.cn

Authors

Zekun Wu - State Key Laboratory of Chemical Engineering, Tianjin Key Laboratory of Applied Catalysis, Science and Technology, School of Chemical Engineering and Technology, Tianjin University, Tianjin 300072, China; Collaborative Innovation Center of Chemical Science and Engineering (Tianjin), Tianjin 300072, China.

Tianzuo Wang - School of Chemical Engineering and Technology, Tianjin University, Tianjin 300072, China; Collaborative Innovation Center of Chemical Science and Engineering (Tianjin), Tianjin 300072, China.

Yongdan Li - State Key Laboratory of Chemical Engineering, Tianjin Key Laboratory of Applied Catalysis, Science and Technology, School of Chemical Engineering and Technology, Tianjin University, Tianjin 300072, China; Collaborative Innovation Center of Chemical Science and Engineering (Tianjin), Tianjin 300072, China; Department of Chemical and Metallurgical Engineering, School of Chemical Engineering, Aalto University, Kemistintie 1, Espoo, P.O. Box 16100, FI-00076, Aalto, Finland.

Z. Wu and T. Wang contributed equally.

Notes

The authors declare no competing financial interest.

Supporting Information

The Supporting Information is available free of charge via the Internet at <http://pubs.acs.org>.

FTIR spectra of NiO_x-C; SEM images of pristine carbon; SEM images of NiO_x-C calcined at different temperatures and corresponding elemental mapping; catalytic performance of 20% NiO_x-C with C being pyrolyzed at 650-800 °C; catalytic performance of NiO_x-C with the loading of Ni varying at 0-40%; catalytic performance of MO_x-C; catalytic performance of glassy carbon; Tafel slope of C, NiO_x-C calcined at different temperatures and MO_x-C; pore properties of pristine carbon pyrolyzed at 650-800 °C; catalytic performance of MO_x-C, and 2e-ORR catalytic performance comparison.

ACKNOWLEDGMENTS

This work was funded by the National Natural Science Foundation of China (Grant No. 51702230).

REFERENCES

- (1) Jiang, Y.; Ni, P.; Chen, C.; Lu, Y.; Yang, P.; Kong, B.; Fisher, A.; Wang, X. Selective Electrochemical H₂O₂ Production through Two-Electron Oxygen Electrochemistry. *Adv. Energy Mater.* **2018**, *8*, 1801909.
- (2) Sun, Y.; Han, L.; Strasser, P. A Comparative Perspective of Electrochemical and Photochemical Approaches for Catalytic H₂O₂ Production. *Chem. Soc. Rev.* **2020**, *49*, 6605-6631.
- (3) Yang, S.; Verdager-Casadevall, A.; Arnarson, L.; Silvio, L.; Colic, V.; Frydendal, R.; Rossmeisl, J.; Chorkendorff, I.; Stephens, I. E. L. Toward the Decentralized Electrochemical Production of H₂O₂: A Focus on the Catalysis. *ACS Catal.* **2018**, *8*, 4064-4081.
- (4) Jiang, K.; Zhao, J.; Wang, H. Catalyst Design for Electrochemical Oxygen Reduction toward Hydrogen Peroxide. *Adv. Funct. Mater.* **2020**, *30*, 20033221.
- (5) Siahrostami, S.; Verdager-Casadevall, A.; Karamad, M.; Deiana, D.; Malacrida, P.; Wickman, B.; Escudero-Escribano, M.; Paoli, E. A.; Frydendal, R.; Hansen, T. W.; Chorkendorff, I.; Stephens, I. E. L.; Rossmeisl, J. Enabling Direct H₂O₂ Production Through Rational Electrocatalyst Design. *Nat. Mater.* **2014**, *13*, 1137-1143.
- (6) Wang, X.; Li, Z.; Qu, Y.; Yuan, T.; Wang, W.; Wu, Y.; Li, Y. Review of Metal Catalysts for Oxygen Reduction Reaction: From Nanoscale Engineering to Atomic Design. *Chem* **2019**, *5*, 1486-1511.
- (7) Lu, Y.; Jiang, Y.; Gao, X.; Chen, W. Charge State-dependent Catalytic Activity of [Au₂₅(SC₁₂H₂₅)₁₈] Nanoclusters for the Two-Electron Reduction of Dioxygen to Hydrogen Peroxide. *Chem. Commun.* **2014**, *50*, 8464-8467.
- (8) Yang, S.; Kim, J.; Tak, Y. J.; Soon, A.; Lee, H. Single-Atom Catalyst of Platinum Supported on Titanium Nitride for Selective Electrochemical Reactions. *Angew. Chem. Int. Ed.* **2016**, *55*, 2058-2062.
- (9) Jirkovský, J. S.; Panas, I.; Ahlberg, E.; Halasa, M.; Romani, S.; Schiffrin, D. J. Single Atom Hot-Spots at Au-Pd Nanoalloys for Electrocatalytic H₂O₂ Production. *J. Am. Chem. Soc.* **2011**, *133*, 19432-19441.
- (10) Zheng, Z.; Ng, Y. H.; Wang, D.; Amal, R. Epitaxial Growth of Au-Pt-Ni Nanorods for Direct High Selectivity H₂O₂ Production. *Adv. Mater.* **2016**, *28*, 9949-9955.
- (11) Li, B.; Zhao, C.; Liu, J.; Zhang, Q. Electrosynthesis of Hydrogen Peroxide Synergistically Catalyzed by Atomic Co-N_x-C Sites and Oxygen Functional Groups in Noble-Metal-Free Electrocatalysts. *Adv. Mater.* **2019**, *31*, 1808173.
- (12) Sun, Y.; Silvioli, L.; Sahaie, N. R.; Ju, W.; Li, J.; Zitolo, A.; Li, S.; Bagger, A.; Arnarson, L.; Wang, X.; Moeller, T.; Bernsmeier, D.; Rossmeisl, J.; Jaouen, F.; Strasser, P. Activity-Selectivity Trends in the Electrochemical Production of Hydrogen Peroxide over Single-Site Metal-Nitrogen-Carbon Catalysts. *J. Am. Chem. Soc.* **2019**, *141*, 12372-12381.
- (13) Jiang, K.; Back, S.; Akey, A. J.; Xia, C.; Hu, Y.; Liang, W.; Schaak, D.; Stavitski, E.; Norskov, J. K.; Siahrostami, S.; Wang, H. Highly Selective Oxygen Reduction to Hydrogen Peroxide on Transition Metal Single Atom Coordination. *Nat. Commun.* **2019**, *10*, 3997.
- (14) Lu, Z.; Chen, G.; Siahrostami, S.; Chen, Z.; Liu, K.; Xie, J.; Liao, L.; Wu, T.; Lin, D.; Liu, Y.; Jaramillo, T. F.; Norskov, J. K.; Cui, Y. High-Efficiency Oxygen Reduction to Hydrogen Peroxide Catalysed by Oxidized Carbon Materials. *Nat. Catal.* **2018**, *1*, 156-162.
- (15) Wang, M.; Zhang, N.; Feng, Y.; Hu, Z.; Shao, Q.; Huang, X. Partially Pyrolyzed Binary Metal-Organic Framework Nanosheets for Efficient Electrochemical Hydrogen Peroxide Synthesis. *Angew. Chem. Int. Ed.* **2020**, *59*, 14373-14377.
- (16) Carneiro, J. F.; Paulo, M. J.; Sijaj, M.; Tavares, A. C.; Lanza, M. R. V. Nb₂O₅ Nanoparticles Supported on Reduced Graphene Oxide Sheets as Electrocatalyst for the H₂O₂ Electrogeneration. *J. Catal.* **2015**, *332*, 51-61.
- (17) Barros, W. R. P.; Wei, Q.; Zhang, G.; Sun, S.; Lanza, M. R. V.; Tavares, A. C. Oxygen Reduction to Hydrogen Peroxide on Fe₃O₄ Nanoparticles Supported on Printex Carbon and Graphene. *Electrochim. Acta* **2015**, *162*, 263-270.

- (18) Assumpcao, M.; Rascio, D.; Ladeia, J.; De Souza, R.; Neto, E. T.; Calegario, M.; Oliveira, R.; Gaubeur, I.; Lanza, M.; Santos, M. Comparative Study of Different Methods for the Preparation of $\text{Co}_x\text{O}_y/\text{C}$ for the Electrosynthesis of Hydrogen Peroxide. *Int. J. Electrochem. Sci.* **2011**, *6*, 1586-1596.
- (19) Assumpção, M.; Moraes, A.; De Souza, R.; Calegario, M.; Lanza, M.; Leite, E.; Cordeiro, M.; Hammer, P.; Santos, M. C. d. Influence of the Preparation Method and the Support on H_2O_2 Electrogenation Using Cerium Oxide Nanoparticles. *Electrochim. Acta* **2013**, *111*, 339-343.
- (20) Zhou, W.; Xie, L.; Gao, J.; Nazari, R.; Zhao, H.; Meng, X.; Sun, F.; Zhao, G.; Ma, J. Selective H_2O_2 Electrosynthesis by O-Doped and Transition-Metal-O-Doped Carbon Cathodes via O_2 Electroreduction: A Critical Review. *Chem. Eng. J.* **2021**, *410*, 128368.
- (21) Zhou, Y.; Chen, G.; Zhang, J. A Review of Advanced Metal-Free Carbon Catalysts for Oxygen Reduction Reactions Towards the Selective Generation of Hydrogen Peroxide. *J. Mater. Chem. A* **2020**, *8*, 20849-20869.
- (22) Zhang, J.; Zhang, H.; Cheng, M.; Lu, Q. Tailoring the Electrochemical Production of H_2O_2 : Strategies for the Rational Design of High-Performance Electrocatalysts. *Small* **2020**, *16*, 1902845.
- (23) Smith, R. D. L.; Prevot, M. S.; Fagan, R. D.; Zhang, Z.; Sedach, P. A.; Siu, M. K. J.; Trudel, S.; Berlinguette, C. P. Photochemical Route for Accessing Amorphous Metal Oxide Materials for Water Oxidation Catalysis. *Science* **2013**, *340*, 60-63.
- (24) Zhang, C.; Zhang, X.; Daly, K.; Bedinguette, C. P.; Trudel, S. Water Oxidation Catalysis: Tuning the Electrocatalytic Properties of Amorphous Lanthanum Cobaltite through Calcium Doping. *ACS Catal.* **2017**, *7*, 6385-6391.
- (25) Pan, L.; Wang, Q.; Li, Y.; Zhang, C. Amorphous Cobalt-cerium Binary Metal Oxides as High Performance Electrocatalyst for Oxygen Evolution Reaction. *J. Catal.* **2020**, *384*, 14-21.
- (26) Wang, Q.; Li, Y.; Zhang, C. Amorphous Nickel Oxide as Efficient Electrocatalyst for Urea Oxidation Reaction. *J. Electrochem. Soc.* **2021**, *168*, 076502.
- (27) Li, X.; Cai, W.; Li, D.; Xu, J.; Tao, H.; Liu, B. Amorphous Alloys for Electrocatalysis: The Significant Role of the Amorphous Alloy Structure. *Nano Res.* **2021**, 1-12.
- (28) Wang, Y.; Gurses, S.; Felyey, N.; Boubnov, A.; Mao, S.; Kronawitter, C. X. In Situ Deposition of Pd during Oxygen Reduction Yields Highly Selective and Active Electrocatalysts for Direct H_2O_2 Production. *ACS Catal.* **2019**, *9*, 8453-8463.
- (29) Liu, M.; Zhang, H.; Li, Y.; Su, H.; Zhou, W.; Zhao, X.; Cheng, W.; Liu, Q. Crystallinity Dependence for High-Selectivity Electrochemical Oxygen Reduction to Hydrogen Peroxide. *Chem. Commun.* **2020**, *56*, 5299-5302.
- (30) Dong, K.; Liang, J.; Wang, Y.; Ren, Y.; Xu, Z.; Zhou, H.; Li, L.; Liu, Q.; Luo, Y.; Li, T. Plasma-Induced Defective TiO_{2-x} with Oxygen Vacancies: A High-Active and Robust Bifunctional Catalyst toward H_2O_2 Electrosynthesis. *Chem Catal.* **2021**, *1*, 1437-1448.
- (31) Li, R.; Yang, S.; Zhang, Y.; Yu, G.; Wang, C.; Chen, C.; Wu, G.; Sun, R.; Wang, G.; Zheng, X. Short-Range Order in Amorphous Nickel Oxide Nanosheets Enables Selective and Efficient Electrochemical Hydrogen Peroxide Production. *Cell Rep. Phys. Sci.* **2022**, *3*, 100788.
- (32) Sevilla, M.; Fuertes, A. B. A General and Facile Synthesis Strategy Towards Highly Porous Carbons: Carbonization of Organic Salts. *J. Mater. Chem. A* **2013**, *1*, 13738-13741.
- (33) Trudel, S.; Crozier, E. D.; Gordon, R. A.; Budnik, P. S.; Hill, R. H. X-ray Absorption Fine Structure Study of Amorphous Metal Oxide Thin Films Prepared by Photochemical Metalorganic Deposition. *J. Solid State Chem.* **2011**, *184*, 1025-1035.
- (34) Zhang, C.; Fagan, R. D.; Smith, R. D. L.; Moore, S. A.; Berlinguette, C. P.; Trudel, S. Mapping The Performance of Amorphous Ternary Metal Oxide Water Oxidation Catalysts Containing Aluminium. *J. Mater. Chem. A* **2015**, *3*, 756-761.
- (35) Kresse, G.; Hafner, J. Ab Initio Molecular Dynamics for Liquid Metals. *Phys. Rev. B* **1993**, *47*, 558.
- (36) Perdew, J. P.; Burke, K.; Ernzerhof, M. Generalized Gradient Approximation Made Simple. *Phys. Rev. Lett.* **1997**, *78*, 1396.
- (37) Perdew, J. P.; Burke, K.; Ernzerhof, M. Generalized Gradient Approximation Made Simple. *Phys. Rev. Lett.* **1996**, *77*, 3865.
- (38) Cramer, C. J.; Truhlar, D. G. Implicit Solvation Models: Equilibria, Structure, Spectra, and Dynamics. *Chem. Rev.* **1999**, *99*, 2161-2200.
- (39) Tomasi, J.; Mennucci, B.; Cammi, R. Quantum Mechanical Continuum Solvation Models. *Chem. Rev.* **2005**, *105*, 2999-3094.
- (40) Grimme, S.; Antony, J.; Ehrlich, S.; Krieg, H. A Consistent and Accurate Ab Initio Parametrization of Density Functional Dispersion Correction (DFT-D) for the 94 Elements H-Pu. *J. Chem. Phys.* **2010**, *132*, 154104.
- (41) Song, X.; Li, N.; Zhang, H.; Wang, L.; Yan, Y.; Wang, H.; Wang, L.; Bian, Z. Graphene-Supported Single Nickel Atom Catalyst for Highly Selective and Efficient Hydrogen Peroxide Production. *ACS Appl. Mater. Interfaces* **2020**, *12*, 17519-17527.
- (42) Kim, H. W.; Ross, M. B.; Kornienko, N.; Zhang, L.; Guo, J.; Yang, P.; McCloskey, B. D. Efficient Hydrogen Peroxide Generation Using Reduced Graphene Oxide-Based Oxygen Reduction Electrocatalysts. *Nat. Catal.* **2018**, *1*, 282-290.
- (43) Liu, Y.; Quan, X.; Fan, X.; Wang, H.; Chen, S. High-Yield Electrosynthesis of Hydrogen Peroxide from Oxygen Reduction by Hierarchically Porous Carbon. *Angew. Chem. Int. Ed.* **2015**, *54*, 6837-6841.
- (44) Gorlin, Y.; Chung, C.; Nordlund, D.; Clemens, B. M.; Jaramillo, T. F. Mn_3O_4 Supported on Glassy Carbon: An Active Non-Precious Metal Catalyst for the Oxygen Reduction Reaction. *ACS Catal.* **2012**, *2*, 2687-2694.
- (45) Cordeiro-Junior, P. J. M.; Kronka, M. S.; Goulart, L. A.; Verissimo, N. C.; Mascaro, L. H.; Mauro, C. D. S.; Bertazzoli, R.; Marcos, R. D. V. L. Catalysis of Oxygen Reduction Reaction for H_2O_2 Electrogenation: The Impact of Different Conductive Carbon Matrices and Their Physicochemical Properties. *J. Catal.* **2020**, *392*, 56-68.
- (46) Chen, S.; Chen, Z.; Siahrostami, S.; Kim, T. R.; Nordlund, D.; Sokaras, D.; Nowak, S.; To, J. W. F.; Higgins, D.; Sinclair, R.; Nørskov, J. K.; Jaramillo, T. F.; Bao, Z. Defective Carbon-Based Materials for the Electrochemical Synthesis of Hydrogen Peroxide. *ACS Sustain. Chem. Eng.* **2018**, *6*, 311-317.
- (47) Huang, J.; Chen, J.; Fu, C.; Cai, P.; Li, Y.; Cao, L.; Liu, W.; Yu, P.; Wei, S.; Wen, Z.; Li, J. 2D Hybrid of Ni-LDH Chips on Carbon Nanosheets as Cathode of Zinc-Air Battery for Electrocatalytic Conversion of O_2 into H_2O_2 . *ChemSusChem* **2020**, *13*, 1496-1503.
- (48) Wang, Y.; Shi, R.; Shang, L.; Waterhouse, G. I. N.; Zhao, J.; Zhang, Q.; Gu, L.; Zhang, T. High-Efficiency Oxygen Reduction to Hydrogen Peroxide Catalyzed by Nickel Single-Atom

Catalysts with Tetradentate N_2O_2 Coordination in a Three-Phase Flow Cell. *Angew. Chem. Int. Ed.* **2020**, *59*, 13057-13062.

(49) Ma, F.; Wang, S.; Liang, X.; Wang, C.; Tong, F.; Wang, Z.; Wang, P.; Liu, Y.; Dai, Y.; Zheng, Z.; Huang, B. Ni_3B as a Highly Efficient and Selective Catalyst for The Electrosynthesis of Hydrogen Peroxide. *Appl. Catal., B.* **2020**, *279*, 119371.

(50) Ren, M.; Lei, J.; Zhang, J.; Yakobson, B. I.; Tour, J. M. Tuning Metal Elements in Open Frameworks for Efficient Oxygen Evolution and Oxygen Reduction Reaction Catalysts. *ACS Appl. Mater. Interfaces* **2021**, *13*, 42715-42723.

(51) Anantharaj, S.; Karthik, P. E.; Noda, S. The significance of properly reporting turnover frequency in electrocatalysis research. *Angew. Chem. Int. Ed.* **2021**, *60*, 23051-23067.

(52) Choi, C. H.; Kwon, H. C.; Yook, S.; Shin, H.; Kim, H.; Choi, M. Hydrogen Peroxide Synthesis via Enhanced Two-Electron Oxygen Reduction Pathway on Carbon-Coated Pt Surface. *J. Phys. Chem. C* **2014**, *118*, 30063-30070.

(53) Park, J.; Nabaee, Y.; Hayakawa, T.; Kakimoto, M. A. Highly Selective Two-Electron Oxygen Reduction Catalyzed by Mesoporous Nitrogen-Doped Carbon. *ACS Catal.* **2014**, *4*, 3749-3754.

(54) Koper, M. T. Thermodynamic Theory of Multi-electron Transfer Reactions: Implications for Electrocatalysis. *J. Electroanal. Chem.* **2011**, *660*, 254-260.

(55) Rüetschi, P.; Delahay, P. Influence of Electrode Material on Oxygen Overvoltage: A Theoretical Analysis. *J. Chem. Phys.* **1955**, *23*, 556-560.

(56) Conway, B.; Bockris, J. O. M. Electrolytic Hydrogen Evolution Kinetics and Its Relation to the Electronic and Adsorptive Properties of the Metal. *J. Chem. Phys.* **1957**, *26*, 532-541.

(57) Yan, B.; Krishnamurthy, D.; Hendon, C. H.; Deshpande, S.; Surendranath, Y.; Viswanathan, V. Surface Restructuring of Nickel Sulfide Generates Optimally Coordinated Active Sites for Oxygen Reduction Catalysis. *Joule* **2017**, *1*, 600-612.

(58) Yeager, E. Dioxygen Electrocatalysis: Mechanisms in Relation to Catalyst Structure. *J. Mol. Catal.* **1986**, *38*, 5-25.

(59) Wang, M.; Dong, X.; Meng, Z.; Hu, Z.; Lin, Y.; Peng, C.; Wang, H.; Pao, C.; Ding, S.; Li, Y.; Shao, Q.; Huang, X. An Efficient Interfacial Synthesis of Two-Dimensional Metal-Organic Framework Nanosheets for Electrochemical Hydrogen Peroxide Production. *Angew. Chem. Int. Ed.* **2021**, *60*, 11190-11195.

(60) Holewinski, A.; Linic, S. Elementary Mechanisms in Electrocatalysis: Revisiting the ORR Tafel Slope. *J. Electrochem. Soc.* **2012**, *159*, H864-H870.

(61) Zhang, C.; Berlinguette, C. P.; Trudel, S. Water Oxidation Catalysis: An Amorphous Quaternary Ba-Sr-Co-Fe Oxide as A Promising Electrocatalyst for the Oxygen-Evolution Reaction. *Chem. Commun.* **2016**, *52*, 1513-1516.

(62) Gao, R.; Wang, J.; Huang, Z.; Zhang, R.; Wang, W.; Pan, L.; Zhang, J.; Zhu, W.; Zhang, X.; Shi, C.; Lim, J.; Zou, J. Pt/ Fe_2O_3 with Pt-Fe Pair Sites as A Catalyst for Oxygen Reduction with Ultralow Pt Loading. *Nat. Energy* **2021**, *6*, 614-623.

(63) Gao, R.; Pan, L.; Li, Z.; Shi, C.; Yao, Y.; Zhang, X.; Zou, J. Engineering Facets and Oxygen Vacancies over Hematite Single Crystal for Intensified Electrocatalytic H_2O_2 Production. *Adv. Funct. Mater.* **2020**, *30*, 1910539.